Eur. J. Mineral., 38, 431–448, 2026
https://doi.org/10.5194/ejm-38-431-2026

European Journal of Mineralogy
Open Access

Fluorine-induced melting in the Ihalainen calcite-wollastonite marble deposit, Lappeenranta, Finland

Robert F. Martin[1], **Dirk Schumann**[2], **Markku J. Lehtinen**[3], **and Sebastian Fuchs**[4]

[1]Department of Earth and Planetary Sciences, McGill University, 3450 University Street, Montreal, Quebec H3A 0E8, Canada
[2]Fibics Incorporated, 1431 Merivale Road, Ottawa, Ontario K2E 0B9, Canada
[3]Geomin & Materials Consulting, Rinnetie 49, 53650 Lappeenranta, Finland
[4]Federal Institute for Geosciences and Natural Resources (BGR), Stilleweg 2, 30655 Hanover, Germany

Correspondence: Robert F. Martin (robert.martin@mcgill.ca)

Received: 29 December 2025 – Revised: 10 April 2026 – Accepted: 1 June 2026 – Published: 20 July 2026

Abstract. Located adjacent to Lappeenranta in southeastern Finland, the Ihalainen marble deposit has operated continuously since 1910. Regional metamorphism of the calcitic and dolomitic marble of the Ihalainen Formation led to wollastonite formation, well dated at 1.86 Ga. At about 1.6 Ga, the area experienced intrusion by the Wiborg batholith of anorogenic granite with a rapakivi texture. Dikes of granite, composite basic–felsic dikes, and dikelets with an aplitic texture intruded into the wollastonite deposit, now part of a roof pendant, and caused localized fluxed melting of the ore. The gaseous transfer of CaF_2 into the heated ore caused a very strange melt to form. It congealed quickly to forsterite, diopside, and graphically intergrown wollastonite + fluorite. Closer to the contact, an injection of geochemically evolved granitic melt induced anatexis of the marble. We investigated an emulsion of the two melts, one desilicated and now syenitic, the other a carbonate melt that contained dissolved silicates. The syenitic melt eventually crystallized to a sanidine solid-solution that underwent spinodal decomposition into two strained feldspars in the presence of a carbothermal fluid. A later influx of an aqueous fluid caused recrystallization of the feldspars but left intact the striking textural evidence of a once-coherent intergrowth. It also led to a bewildering array of calcic secondary minerals like pectolite, grosssular, holtstamite, and lawsomite. Three undescribed minerals in the affected rocks contain the high-field-strength elements Sn, Nb, and Ta.

1 Introduction

Ihalainen is a major marble-hosted deposit of wollastonite located at Lappeenranta, southeastern Finland. It occurs close to the Lappee rapakivi granite, part of the anorogenic Wiborg batholith. Much of the wollastonite mineralization at Ihalainen had formed roughly 300×10^6 years before the emplacement of the batholith. The Wiborg batholith typically exhibits high levels of fluorine and, locally, also of U, Th, and Be (Rämö, 1991). The block of marble, now largely surrounded by granitic rocks, is interpreted to be a roof pendant, one of several encountered in the batholith (Vorma, 1975).

The Ihalainen site has been exploited since the 1500s and continuously so since 1910 (Lehtinen, 1999). Owing to the mining of the deposit, the geological context, to be reviewed below, is well understood. Markku Lehtinen was employed as a mine and production geologist from 1990 to 1999 (Partek Minerals Oy Ab) and further from 2007 to 2018 (Nordkalk Corporation). He wrote his Ph.lic. thesis (1995) on the mineralogy and geology of the Ihalainen Formation. The other authors have joined forces with him to shed further light on the texture and composition of the essential minerals in five specimens of wollastonite ore, three of which are described in Lehtinen (1995). Our results, acquired with high-resolution scanning electron microscopy

with energy-dispersion spectrometry, are supplemented with electron-microprobe analyses of some exotic phases that may be new species of minerals. The intrusion of the fluorine-rich granitic magma caused fluxed melting of the ore assemblage. We focus on the two specimens in which aplitic dikelets are visible.

2 Background information

Wiborgite (rapakivi granite), a more mafic equigranular granite, and porphyritic biotite granite form the wallrocks of the roof pendant (Vorma, 1964). Near Lappeenranta, the roof pendant has a north–south strike and measures roughly 3×0.8 km. The Ihalainen open pit is 1.2 km long with a maximum width of 450 m and depth of 120 m (Fig. 1). The structure is rather simple; the strata have a 65° E dip. The simplified geological map (Fig. 1a) is adapted from maps 3133 of Simonen (1979) and 3134 of Vorma (1964). The white marble (Paleoproterozoic, 1.9 Ga) consists predominantly of calcite marble with areas of concordant strata of dolomitic marble, each originally containing quartz and silicates as detrital minerals. Calcite is the main economic mineral of this mine. Wollastonite is mined principally from a zone containing wollastonite + diopside ± quartz in a matrix of coarse-grained calcite, commonly bluish in color.

The wollastonite ore was formed in two metamorphic events (Lehtinen, 1995). First, there was the regional episode, during which the area attained a temperature of 650–700 °C at a pressure estimated to be 500 MPa (Kilpeläinen and Rastas, 1992). Radiometric dating of titanite establishes the age of that event at 1.858 ± 0.020 Ga. That is when the main wollastonite-rich zones formed, in places where H_2O infiltrated the original relatively siliceous horizons in the original limestone. The dilution of the CO_2 concentration in the fluid phase promoted the crystallization of wollastonite as a member of a regional metamorphic assemblage.

Roughly 300×10^6 years later, a lower-pressure episode of reheating at approximately 1.6 Ga coincided with the engulfing of the roof pendant in granitic magma. Near the contacts with the rapakivi granite, massive to semi-massive wollastonite skarns developed with a wollastonite content of up to 30 vol. % or more. Cordierite–spinel pairs from migmatite at the western contact of the batholith give an equilibrium temperature of 660 °C (Lehtinen, 1999). An influx of basic magma feeding diabase dikes marks the onset of the emplacement of the rapakivi granite in the area (Rämö, 1991). Composite basic–felsic dikes, with a granitic core and a basic rim, show that felsic and basic magmas were both coevally available in the area. The rapakivi granite had surprisingly little visible effect on the marble along contacts (Lehtinen, 1999). In his thesis, Lehtinen (1995) documented the presence of aplitic veinlets and listed approximately 60 minerals in the ore assemblage, including late-stage minerals like serpentine, talc, sepiolite, fluorite, fluorapophyllite, pectolite, prehnite, and graphite.

3 Materials and methods

We acquired large-area transmitted-light image mosaics from five polished thin sections using a Zeiss AXIO Zoom.V16 light microscope. Samples MKL-1028B, MKL-1066, and ML-1A are used to describe the typical wollastonite ore (Fig. 2), whereas MKL-1021 and ML-3A, the focus of this article, will be described in detail. The mosaics were acquired with the software ZEN Pro using the Plan Apo Z 0.5/0.125 objective (FWD 114 mm) at a resolution of 811 nm per pixel with transmitted light (TL). Large-area image mosaics were acquired with the ZEISS Atlas 5 software by using a ZEISS EVO MA 15 tungsten filament scanning electron microscope (SEM) at Fibics Incorporated (Ottawa, Canada). The light microscopy mosaics were imported into the respective Atlas 5 correlative workspace projects, aligned with the sample in the microscope, and the large-area SEM image mosaics were acquired using the imaging parameters shown in Table 1. Once the large-area image mosaics were acquired, stitched, and image-corrected, the entire Atlas 5 datasets were exported to an autonomous series of files called the Browser-Based Viewer (BBV), which allows anyone on a PC with a web browser to examine the complete dataset at full resolution. The computer mouse is used to zoom in and out, as well as to navigate through the large-area image mosaic.

Energy-dispersive spectroscopic (EDS) analyses were also carried out on the Zeiss EVO MA 15 tungsten-filament SEM equipped with two Bruker XFlash 6/30 EDS detectors controlled using the Esprit 1.9 software. An accelerating voltage of 20 kV and a probe current of 3.7 nA were used for the acquisition of EDS element distribution maps and point analyses. The element maps and point analyses acquired were exported from the Bruker Esprit software, arranged into figure plates using the software CorelDRAW 2024, exported as PDF or JPG files, and linked with their respective location of acquisition in the Atlas 5 Browser-Based Viewer datasets. The analytical results can be viewed by clicking with the mouse in the green rectangular regions that mark the locations in which the analyses were performed. After clicking, a new browser window will open, and the PDF or the JPG file can be viewed and downloaded.

Selected minerals in two sections showing the strongest influence of the intruding magma, MKL-1021 and ML-3A, were chemically analyzed with a JEOL JXA-8530F field emission electron hyperprobe at the Federal Institute for Geosciences and Natural Resources (BGR) in Hanover, Germany. The analyses were conducted with an electron acceleration of 15 kV; a current of 20 nA; a beam less than 1 µm across; and the following standards: apatite, diopside, hematite, orthoclase, plagioclase, rhodonite, scheelite, tanta-

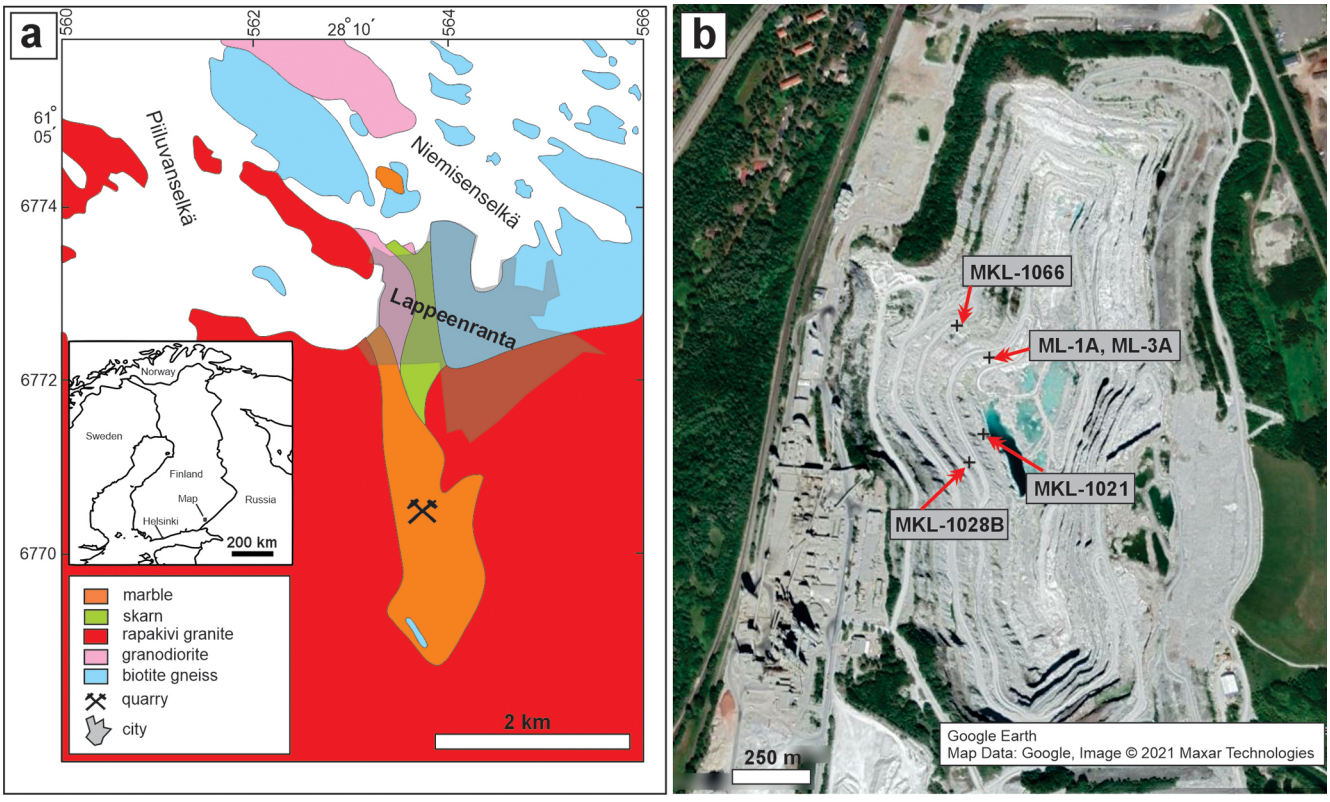

Figure 1. The Ihalainen calcite–wollastonite deposit is located in Lappeenranta, South Karelia region, Finland (61°04′ N, 28°11′ E). **(a)** The simplified geological map, adapted from maps 3133 of Simonen (1979) and 3134 of Vorma (1964), shows the major map units. **(b)** The satellite photo of the open pit indicates the approximate location of the sites sampled.

Table 1. SEM imaging conditions and parameters for specimens from the Ihalainen calcite–wollastonite deposit, Lappeenranta, Finland.

Sample	MKL-1021	MKL-1028B	MKL-1066	ML-1A	ML-3A
Instrument	EVO 15	EVO 15	EVO 15	EVO 15	NVision 40
EHT (kV)	20	20	20	20	18
WD (mm)	10.87	10.57	11.25	11.15	10.84
Beam current (nA) or aperture (µm)	1.7	2.1	1.7	2.1	120 µm
Detector(s)	BSD	BSD	BSD	BSD VPSE G3	KE BSD
Dwell time (µs)	4	4	4	4	3
Resolution (nm per pixel)	200	200	200	200	300
Image size (pixels)	3072 × 3072	3072 × 3072	3072 × 3072	3072 × 3072	2048 × 2048
Image size (µm) (FOV)	614.3 × 614.3	614.3 × 614.3	614.3 × 614.3	614.3 × 614.3	614.3 × 614.3
Image tiles	2435	2958	2701	3122	3151
Mosaic size (gigapixel)	23.0	27.9	25.5	29.5	13.2

EHT: electron high tension; FOV: field of view; WD: working distance.

Figure 2. A sample of typical wollastonite ore (MKL-1066). The coarser tablets of wollastonite have a random orientation. The wavy white layers contain finer-grained wollastonite + diopside.

lite, and Rb–Ti phosphate (synthetic). The spectral lines of the elements used are as follows: $K\alpha$ measured for Si, Ti, Al, Fe, Mg, Ca, Na, K, P, Sc, S, F, and Cl; $L\alpha$ measured for Sr, Sn, Nb, Zr, and Y; and $M\alpha$ measured for W and Ta.

4 Detailed petrography

4.1 Samples of wollastonite ore

Figure 2 illustrates a typical sample of wollastonite ore. The coarse-grained bluish marble contains sinuous white layers of fine-grained wollastonite with diopside and accessory apatite. The conformable layers represent planar accumulations of fine-grained wollastonite + diopside along an undulating plane, likely a bedding plane in the original limestone. Specimens MKL-1066 and MKL-1028B (Fig. 3a, map 8) also show randomly oriented wollastonite crystals overprinting the original layers. The diopside has a Mg# value in the range 96.4 to 97.5 and is aluminous. Those two specimens, along with ML-1A, were likely collected at a distance from the marble–granite contact at depth (i.e., not exposed in the quarry) as they do not contain veins or dikelets attributable to the granite.

The section prepared from MKL-1066 is oriented perpendicular to the layers; the ring-like array of wollastonite and diopside grains (Fig. 3b) results from a cut along a crenulated layer. The wollastonite grains seem oriented with the c axis in the plane of the section and coexist with diopside, graphite, pyrrhotite, quartz, and a K-rich feldspar in a matrix of featureless calcite. It is common to see hydroxylapatite enclosed in wollastonite (Fig. 3c, section ML-1A, map 3). Both hydroxylapatite and diopside are considered to be coeval with wollastonite. The late introduction of quartz and pectolite [$NaCa_2Si_3O_8(OH)$], as well as K-feldspar (Fig. 3b) are likely a distal subtle manifestation of fluid circulation associated with granite emplacement. Figure 3d provides textural evidence of the late growth of quartz. The cavernous crystal of quartz in Fig. 3d (section ML-1A, map 3) is amoeboid and 210 µm across. Quartz grew along calcite grain boundaries and contains tiny islands of wollastonite, as does the calcite. These tiny crystals may also be of a late generation. Table S1a, b, and c in the Supplement list the minerals encountered in sections MKL-1066, MKL-1028B, and ML-1A, respectively.

4.2 Sample MKL-1021

Specimen MKL-1021 is chosen to investigate a narrow dike of fluorite-bearing aplitic material intruding the bluish marble (Fig. 4). The backscattered-electron image mosaic of the thin section (Fig. 5) shows the dikelet in contact with marble along the right edge and the narrow offshoots that penetrated the marble (for PPL and XPL image mosaics, see Figs. S1 and S2). Thirty-five maps were prepared, and results of our petrographic observations are presented in Table S1d. We have selected eight maps to describe the salient features of MKL-1021 (Fig. 6). Maps not used in Fig. 6 can be viewed and downloaded from the Browser-Based Viewer dataset of sample MKL-1021 following the link https://petapixelproject.com/mosaics/geology/Ihalainen/MKL-1021-BBV/index.html (last access: 13 July 2026).

The numbered sites on some maps denote the location of spots analyzed with an electron probe. The dike material at the edge of the section consists of a texturally complex juxtaposition of fine-grained domains of intergrown wollastonite + fluorite in pink and gray-green layers of "aliettite", compositionally similar to lizardite but containing Ca, interpreted to be a breakdown product of forsterite (Fig. 6a, map 6, sites 12–16). The label aplite is used here in a textural sense. Quartz and feldspar are both absent in this section but are present where the dikelet is thicker in the exposure. Grains of fluorite not involved in the micrographic intergrowth (sites 24, 25) and of fluorapophyllite-(K) (sites 17–22) also are present. The entire assemblage is surrounded by a ribbon-like envelope of diopside or wollastonite or fluorite. What was inside the envelope is interpreted to have been a near-eutectic fluorosilicate melt from which either diopside or wollastonite or fluorite could nucleate early upon injection into the calcite host. The constituents of the ribbon represent the minerals formed from the volume of melt as it quenched in contact with the carbonate matrix.

A closeup view of a domain of the wollastonite–fluorite micrographic intergrowth (Fig. 6b, map 2) reveals a preferred orientation of wollastonite and fluorite "rods" growing more or less perpendicular to the edge of the array. Tiny

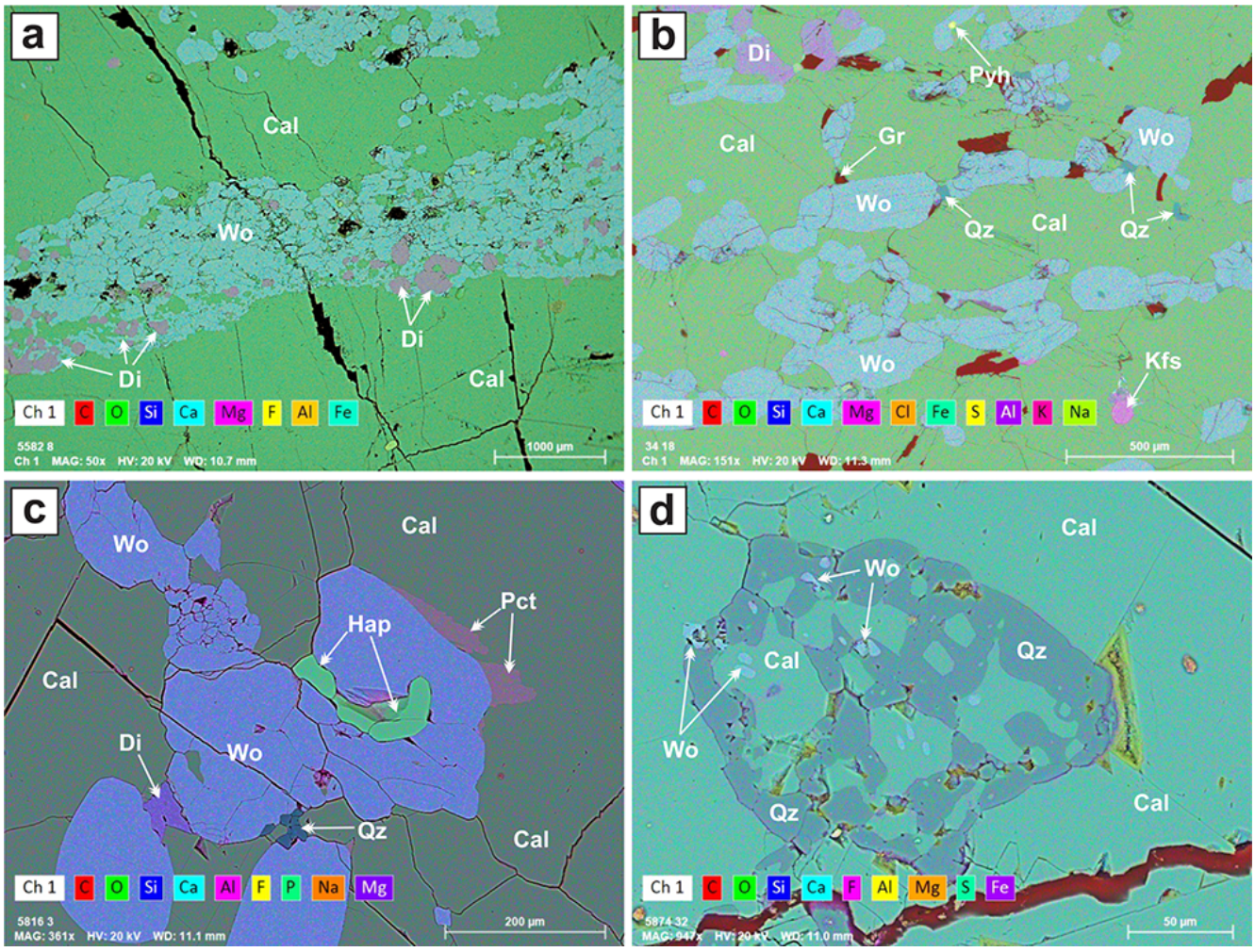

Figure 3. A panel of four labeled maps selected among the available element distribution maps prepared from samples MKL-1066 ($n = 50$ maps, **a**), MKL-1028B ($n = 33$ maps, **b**), and ML-1 ($n = 40$ maps, **c**, **d**) to show typical views of the wollastonite ore and the minerals it contains. The mineral symbols used: Cal – calcite, Di – diopside, Gr – graphite, Hap – hydroxylapatite, Kfs – potassium-rich feldspar, Pct – pectolite, Pyh – pyrrhotite, Qz – quartz, Wo – wollastonite.

grains of scheelite and fluorapatite are present in the center of the array. The "aliettite" (sites 1–4), the fluorapophyllite-(K) (sites 5, 6), and a discrete grain of fluorite (sites 9, 10) are in a peripheral position. Figure 6c (map 9) shows a distal narrow "dikelet" that has congealed in the carbonate matrix. The "aliettite" figures prominently at the periphery (sites 31–35), whereas the wollastonite + fluorite intergrowth is largely within the "aliettite" envelope. The fluorapophyllite-(K) (sites 37–39) is a product of the low-temperature alteration of wollastonite.

Malayaite, the tin analog of titanite, is also present in the wollastonite–fluorite intergrowth (Fig. 6d, map 17, sites 40–43). It locally forms part of the ribbon mentioned above. Its structural formula shows Al, Ti, Nb, Ta, and Zr at the Sn site (Table S2): $(Ca_{1.001}Sr_{0.002}Na_{0.008})_{\Sigma 1.011}(Sn_{0.842}Al_{0.127}Ti_{0.107}Nb_{0.012}Ta_{0.010}Fe_{0.007}Zr_{0.005})_{\Sigma 1.110}Si_{0.995}O_5$. In Fig. 6e (map 25), a grain 25 µm across contains essential Ca, Sn, and S (sites 67–70). It is considered to be a secondary phase because it occurs in a pitted zone in the calcite matrix and because it contains F and Cl (and, thus, likely OH). Its stoichiometry, with Ca : Sn : S of $\approx 4 : 2 : 21$, does not agree with that of genplesite, $Ca_3Sn(SO_4)_2(OH)_6{\cdot}3H_2O$ (Pekov et al., 2018), the only mineral known to contain those elements. With so much sulfur, it could be a mixed sulfide–oxide mineral; we have labeled the unknown mineral UK1.

In another closeup view of an area of the micrographic intergrowth (Fig. 6f, map 34), a rim of diopside, wollastonite, or fluorite (sites 99, 100) encloses a relatively undisturbed area of the intergrown wollastonite + fluorite and a domain of an apophyllite-group mineral containing islands of unreacted wollastonite (sites 91–95) and scattered specks of cassiterite (site 101). Figure 6g (map 33) shows the progressive

Figure 4. Specimen MKL-1021 consists of coarse-grained bluish marble intruded by zoned dikelets of aplitic material. The center of each dikelet is pinkish gray, and the rim is white. The width of the field of view is 7.6 cm.

replacement of wollastonite by the apophyllite-group mineral (sites 71–75).

In Fig. 6h (map 19), there is evidence of a feldspathic inclusion carried by the intruding melt; it has become an assemblage of Ca-free albite and Na-free holtstamite, a hydrogarnet of ideal composition, $Ca_3Al_2(SiO_4)_{3-x}[H_4O_4]_x$ (Table S3, sites 49–50, 52, and 55–56). The K-feldspar, analyzed at sites 53 and 54, contains $K_{95.5}Rb_{1.8}Na_{1.6}Ca_{1.0}Ba_{0.2}$. One of the EDS spectra indicates the presence of a calcium aluminate with a very small Si peak, possibly the hydrogarnet katoite, ideally $Ca_3Al_2\square_3(OH)_{12}$.

At a submagmatic temperature, wollastonite in this environment locally broke down to fluorapophyllite-(K). Twenty-three compositions are listed in Table S4. In all cases, the proportion of F at the anion site exceeds that of OH. Both the Ca and K sites are incompletely filled. The remaining major phase, "aliettite", also appeared at a low temperature. Apart from a small Ca peak, its energy dispersion spectrum is very similar to that of lizardite. The 23 compositions determined by electron microprobe analysis (Table S5) exhibit quite a range of compositions. They are most similar to that of aliettite, ideally a regular interstratification of talc and saponite or trioctahedral smectite (Veniale and van der Marel, 1969; Bailey, 1981). The match is far from perfect, particularly in connection with the Mg : Si ratio, which is too low, and the Ca content, which is high compared to the ideal composition of aliettite. We believe that either more than two modules are involved in the interlayering of the layer silicates or the mixed layering is irregular and possibly random. Further refinements of the true nature of "aliettite" must await X-ray diffraction and infrared absorption analyses. The occurrence of saponite-15 Å has been confirmed at Ihalainen by means of XRD and probe analyses.

The diopside in MKL-1021 (Table S6) is significantly more iron-rich than in the samples mentioned in Sect. 4.1; its Mg# [$= 100Mg/(Mg + Fe^{2+} + Mn)$] value, on average, is 83.7. It contains a small amount of ^{VI}Al, and measurable amounts of tin are present at most of the points analyzed. A subhedral morphology is locally developed, as for fluorapatite.

4.3 Sample ML-3A

4.3.1 The rock-forming minerals

Sample ML-3A is texturally and mineralogically a challenging specimen; 58 areas of interest in the polished thin section were mapped. As in the previous specimen, aplitic dikelets cut the blue marble, with evidence of a decrease in the blue coloration near the dikelets (Fig. 7). The dikelets are zoned, with wollastonite crystals accumulating along the margins, growing outward into the calcite matrix (Figs. 8, S3, and S4). Although the aplitic dikelet is fine-grained, leucocratic, and feldspar-bearing, quartz is absent. Of the 58 maps that were prepared, eight are selected as being representative of the complex assemblages of rock-forming minerals (Fig. 9), and six more focus on the exotic minerals found (Fig. 10). We summarize the mineral assemblages found in each map in Table S7. Maps not used in Figs. 9 and 10 can be viewed and downloaded from the Browser-Based Viewer dataset of sample ML-3A following the link https://petapixelproject.com/mosaics/geology/Ihalainen/ML-3A-BBV/index.html (last access: 13 July 2026).

Figure 9a (map 16) shows the contact area of a typical dikelet. The characteristic accumulation of wollastonite along the rim of the dikelet involves crystals up to 1 mm across that enclose both diopside and calcite. A prominent rim of diopside defines the edge of the wollastonite-enriched zone. The diopside in that rim contains a small amount of tin (~ 0.2 % SnO_2) and has a Mg# value of 97.3, whereas diopside associated with the wollastonite-enriched zone contains no tin and virtually no iron (Mg# = 99.7; Table S8, sites 66 and 67, respectively).

Away from the wollastonite-enriched contact is a fine-grained chilled margin. It consists of a network of interconnected calcite domains that enclose a fine-grained assemblage of the same minerals, as developed in the core of the dikelet. The core assemblage consists of prominent domains of calcite (orange) that partially surround and are included in the silicate minerals. Chief among these are grains of mottled K-feldspar (pale brownish gray, Fig. 9b–f), muscovite (darker green, Fig. 9a–d), and a sodic aluminosilicate (blue). The muscovite, analyzed at EPMA sites 56 to 58 and 62 to 64, contains $K_{0.807}Na_{0.006}Rb_{0.019}Ca_{0.005}Sr_{0.003}$

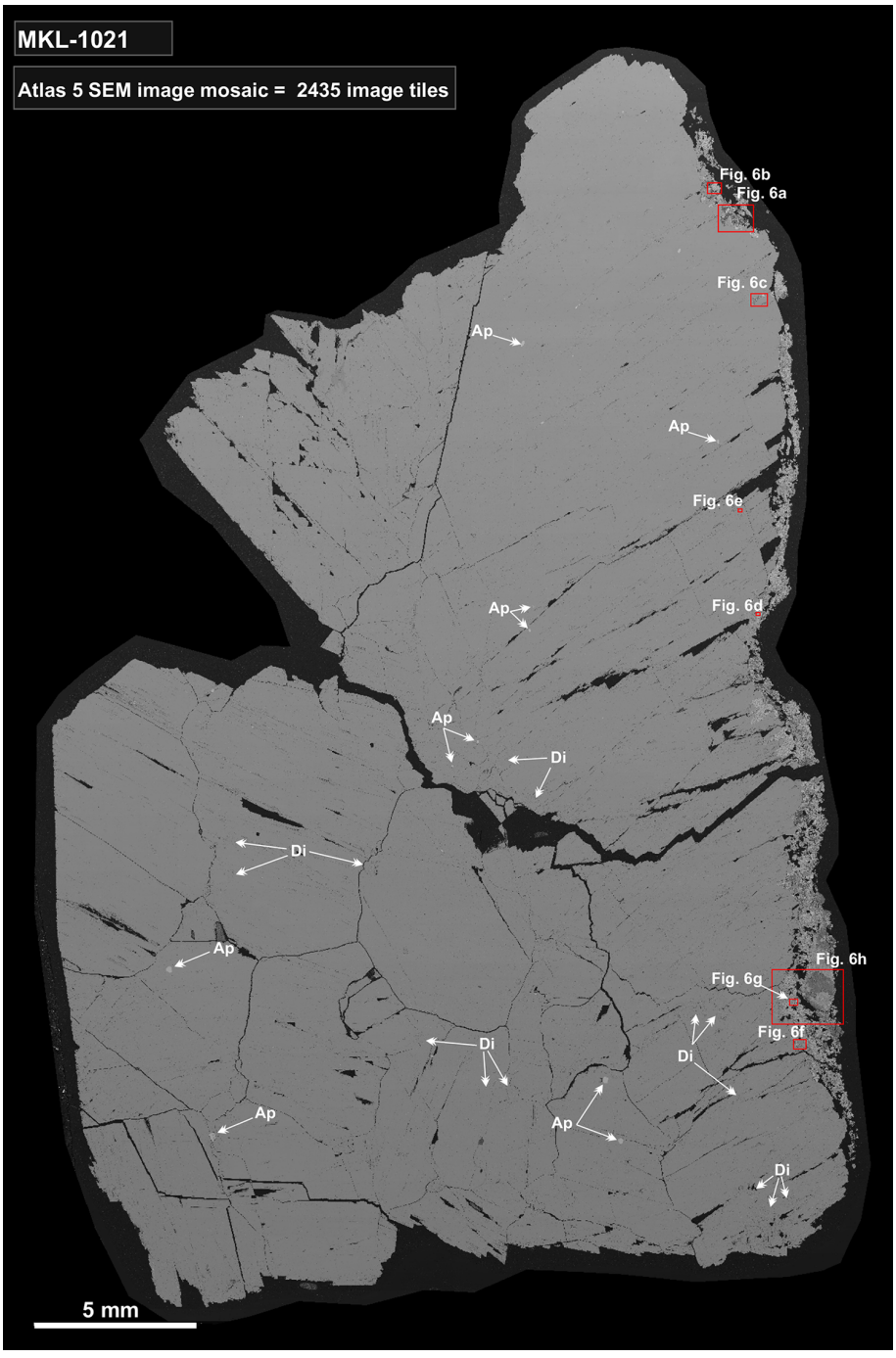

Figure 5. Backscattered-electron image mosaic of section MKL-1021. A dikelet forms the right-hand border of the section. The width of the field of view is roughly 2 cm.

at its interlayer site (Table S9). It is invariably associated with a sodic aluminosilicate, interpreted to be paragonite (Table S10, EPMA site 61). The fine-grained wollastonite in this zone is partially converted to pectolite (Fig. 9e, f; Table S11, site 65) that contains a small proportion of sulfate and phosphate tetrahedra.

The reason for the mottled look of K-feldspar in Fig. 9a becomes evident at higher magnification (Fig. 9b, map 9). The unusual pattern of intergrown feldspars is a result of exsolution of an initially homogeneous alkali feldspar. The width of the elongate lamellae is commonly less than 1 µm; they do not seem crystallographically aligned. Rather, they are oriented roughly perpendicular to the contact with the

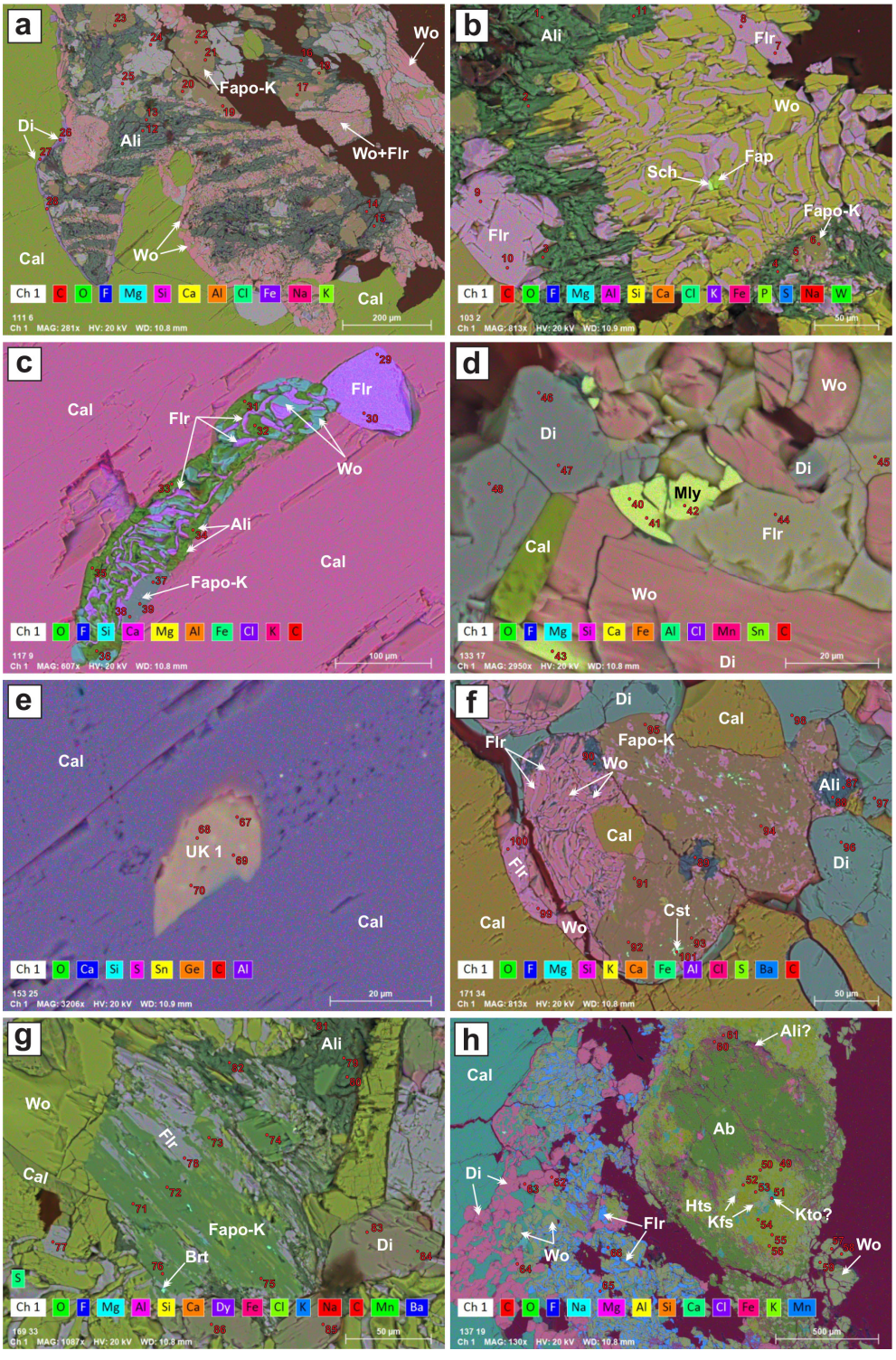

Figure 6. Eight maps (**a** to **h**) are selected to illustrate textural attributes and mineral assemblages in section MKL-1021. The minerals are identified on the basis of their energy dispersion spectrum. The order of crystallization and the minerals present in each of the 35 maps are listed in Table S1d. The map number is the second number in the lower-left corner. Smaller numbers positioned on some maps mark the site of electron microprobe analyses, the results of which are recorded in Tables S2 to S6. The scale is provided on each map.

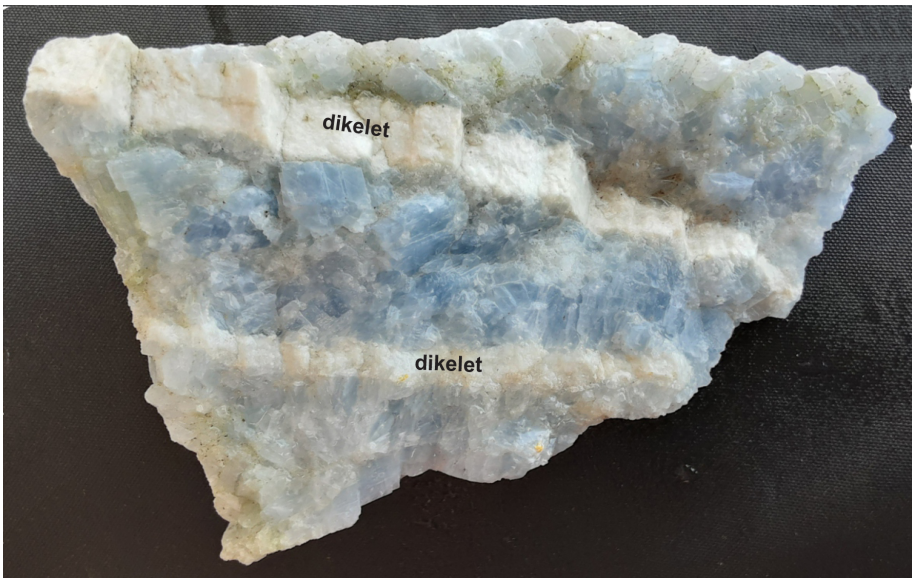

Figure 7. Specimen ML-3A contains white quartz-free aplitic dikelets intrusive in the blue marble host. The width of the field of view is roughly 10 cm.

blob of calcite. The electron beam was broadened during EPMA at sites 1, 2, and 3 to obtain a bulk composition of those areas. The bulk composition of areas 2 and 3 indicates roughly equal proportions of Ab and Or, with minor An (3.0 %, 1.3 %; Table S12). Area 1 gives a more calcic bulk composition (∼ 20 %) at the expense of the albite component, presumably owing to the presence of a calcic alteration product, interpreted to be lawsonite, the only hydrous silicate of Ca, Al, and Si that contains those elements in the same proportions as in anorthite.

The *M* site of the K-feldspar lamellae, measured at sites 4, 8, 9, and 14 (Fig. 9b, Table S13), has an average composition of $K_{0.877}Na_{0.074}Rb_{0.024}Ca_{0.010}Sr_{0.003}$. The adjacent lamellae of albite at sites 6, 7, and 13 are transformed into paragonite (Pg, dark blue). The grains of calcite have an amoeboid shape; EDS spectra invariably show trace amounts of strontium and magnesium. Grains of muscovite are typically anhedral and riddled with inclusions of paragonite. Diopside (site 20) has an Mg# value of 97.2 (Table S8).

Prehnite is present at sites 21, 22, and 23 (Table S14), but the stoichiometry is likely affected by "contamination" owing to overlap by the electron beam on adjacent phases (Fig. 9b). We interpret the mineral at sites 5, 10, and 12 (dark green) to be lawsonite pseudomorphic after albite (Table S15). Holtstamite (Table S16, sites 15–18) forms a partial rim around calcite, along with K-feldspar. Pectolite (Table S11, site 19) has partially replaced wollastonite.

In a higher-magnification view (Fig. 9c, map 23), the lamellar intergrowth of the two feldspars is preferentially oriented perpendicular to the amoeboid grains of calcite. The alkali position of the K-feldspar (sites 40, 41, 44, and 45) contains, on average, $K_{0.809}Na_{0.077}Rb_{0.045}Ca_{0.007}Sr_{0.003}$ (Table S13). The albite lamellae at sites 39 and 42 show the effects of "contamination" due to overlap of the beam with the adjacent phases (16.2 % and 16.0 % "Or", respectively, and 8.7 % "An", likely attributable to a film of lawsonite at site 39: Table S17). The composition of the feldspars at sites 37 and 38 is composite as the electron beam sampled domains of both K-feldspar and albite, possibly also intersecting a film of lawsonite, to account for 4 % An at both sites (Table S12). The Mg# value of diopside at sites 43 and 46 is 95.7 (Table S8).

Another high-magnification view (Fig. 9d, map 3) shows the erratic pattern of the K-feldspar and albite lamellae that developed during unmixing. The alkali position of the K-feldspar (sites 27, 31, and 34) contains, on average, $K_{0.845}Na_{0.072}Rb_{0.022}Ca_{0.009}Sr_{0.002}$ (Table S13) or $Or_{86.7}Ab_{7.2}An_{0.9}$. Paragonite is found at site 26, throughout the large area of intergrown feldspars, and as inclusions in muscovite, accounting for its "moth-eaten" look. The composition recorded at site 29 is hybrid, consisting of 56.1 % Ab, 21.8 % Or, and 21.5 % An, i.e., lawsonite (Table S17). Lawsonite is recorded at site 30 (Table S15) and is responsible for the dark-blue wormy replacement of albite in the intergrowth to the right of the calcite grains (Fig. 9d). The pale-blue mineral at sites 32 and 33 is an aluminosilicate containing Si, Al, Na, Ca, and K in the proportions 8, 7, 2, 1, and 0.8, as well as Cl. We suspect a scapolite solid-solution.

Figure 9e (map 5) shows a more advanced replacement of the albite lamellae by a calcic aluminosilicate and of wollastonite by pectolite. The K-feldspar at site 51 has an Rb-bearing composition similar to those above (Table S13). The sodic plagioclase has been replaced by paragonite near the top of the field of view and by prehnite, analyzed at sites 50

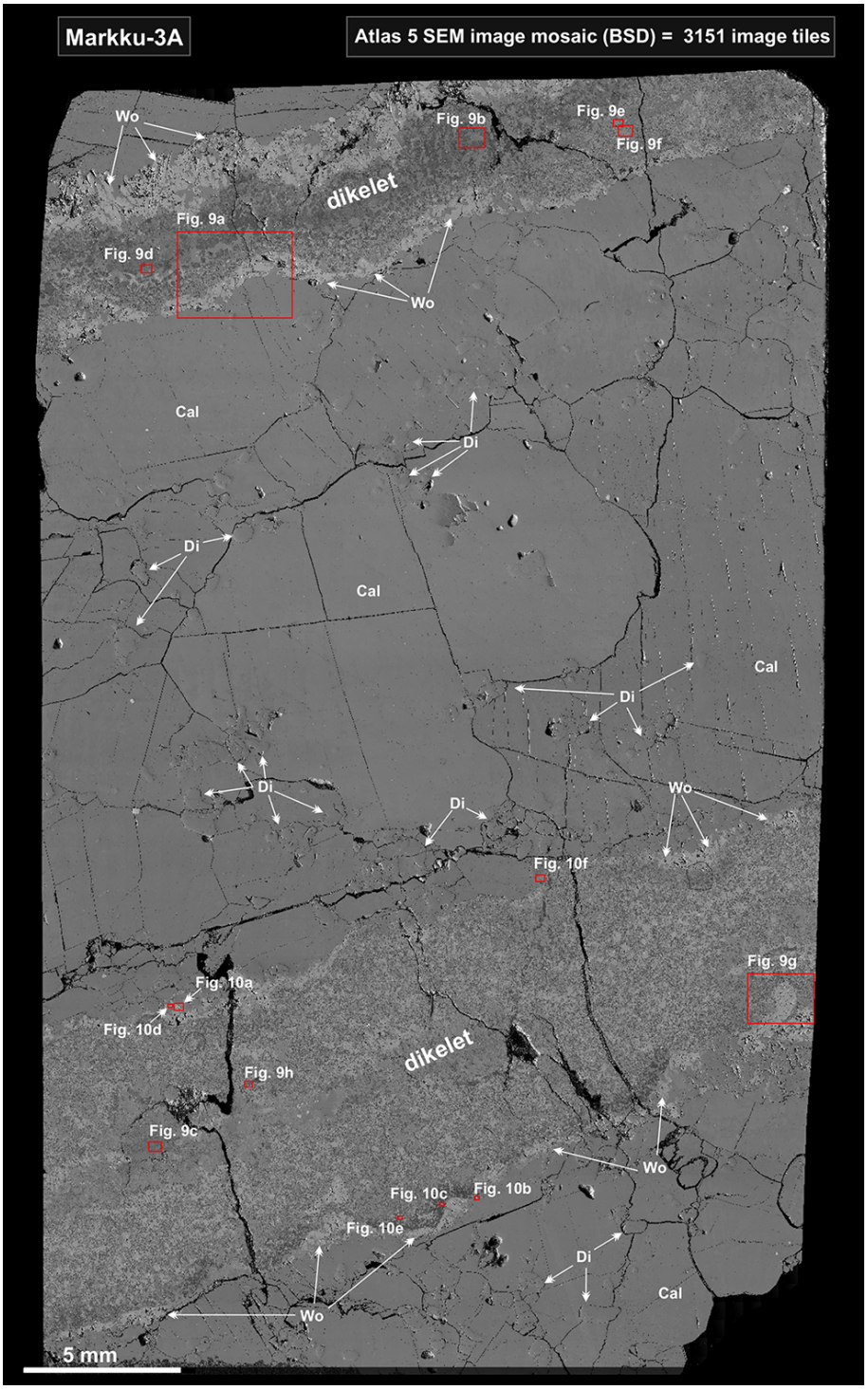

Figure 8. Back-scattered electron image mosaic of section ML-3A. Two zoned dikelets are intersected. Note the buildup of wollastonite crystals along the margins of the dikelets. The width of the field of view is roughly 2 cm.

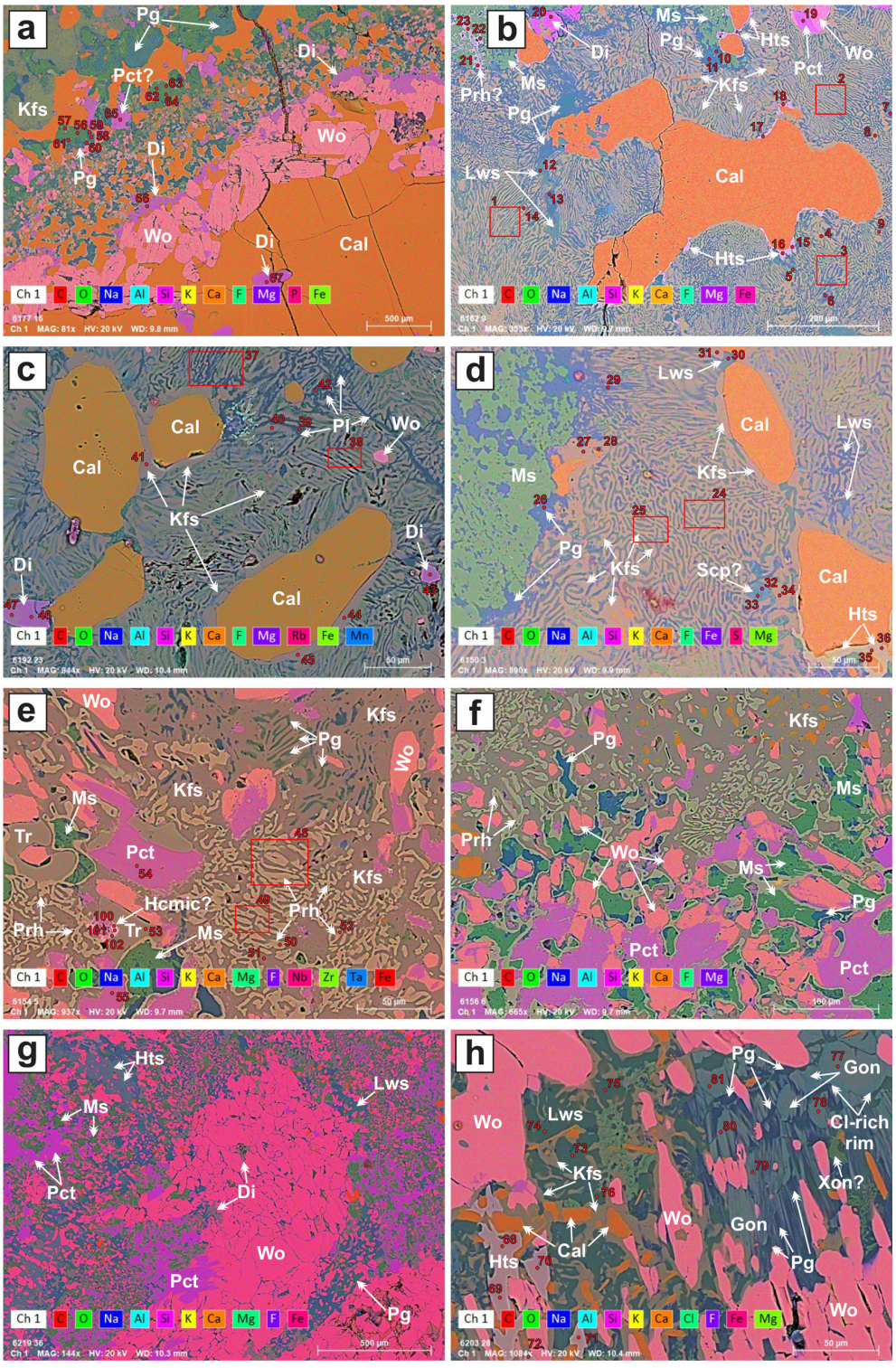

Figure 9. Eight maps (**a** to **h**) are selected to illustrate textural attributes and mineral assemblages in section ML-3A. The minerals are identified on the basis of their energy dispersion spectrum. The order of crystallization and the minerals present in each of the 58 maps are listed in Table S7. The map number is the second number in the lower-left corner. Smaller numbers positioned on some maps mark the site of electron probe analyses, the results of which are recorded in Tables S8 to S22. The scale is provided in each map.

and 52 (Table S14); the compositions are "contaminated" by the adjacent K-feldspar, however. Compositions determined at sites 48, 49, and 52 are provisionally interpreted as mixtures of K-feldspar and prehnite. The composition at site 53 suggests a tremolitic amphibole. In this area where hydrous phases predominate, we suspect the presence of hydroxycalciomicrolite forming a narrow rim on cavernous pectolite (Fig. 9e, sites 100–102). Here also, the electron beam has encroached upon domains of adjacent grains, pectolite and tremolitic amphibole in this case. Tungsten and fluorine are recorded in this tantalum-rich mineral, but niobium is absent.

A continuation of the same theme is seen in Fig. 9f (map 6). The top of the image consists of K-feldspar ($Or_{95.3}Ab_{4.7}$, EDS data) containing small angular inclusions of calcite and wollastonite, along with vestiges of the intergrowth in which the albite component has been replaced by prehnite (?). The bottom half of the image shows a concentration of coarser-grained wollastonite, in part altered to pectolite, associated with muscovite and a sodic phase, likely paragonite.

Map 36 (Fig. 9g) shows a compact accumulation of wollastonite crystals not seen elsewhere in our samples. The cluster seems to have been dislodged; it is surrounded by a fine-grained assemblage of exsolved feldspar + muscovite, now degraded to a mixture of holtstamite, lawsonite, paragonite, and pectolite. Vestiges of a graphic intergrowth involving wollastonite are visible at the center top of the field of view.

In Fig. 9h (map 28), the prominent minerals are wollastonite and a texturally modified exsolution-related assemblage. The K-feldspar in the assemblage is intact, but the sodic plagioclase has been incompletely replaced by lawsonite (sites 73–76, Table S17). An accumulation of wollastonite seems to have been displaced by flowage, and the intervening bluish mineral (sites 77–81) is an aluminosilicate of Ca and Na that maintains the orientation of the wollastonite slivers. Its composition matches closely that of gonnardite, a fibrous zeolite. Its anhydrous composition is $(Ca_{2.404}Na_{0.716}K_{0.138}Sr_{0.003}Y_{0.001})_{\Sigma 3.262}(Al_{4.120}Si_{5.871}S_{0.008}P_{0.001})_{\Sigma 10}O_{20.784}$ (Table S18). Each crystal of gonnardite is zoned outward in chlorine. Gonnardite is intergrown with paragonite (dark blue, labeled Pg), a product of replacement of the sodic plagioclase. Also present in olive green is another Ca–Si replacement phase, interpreted to be xonotlite, $Ca_6Si_6O_{17}(OH)_2$, on the basis of its energy dispersion spectrum.

4.3.2 The exotic species

Next, we present six high-magnification maps that focus on exotic species in the thin section ML-3A. One of these has formed near a fracture among degraded pectolite, holtstamite, and deformed diopside (Fig. 10a, map 30). The diopside, analyzed at sites 94 and 95, has an Mg# value of 96 and contains up to 0.24 % SnO_2 (Table S8). Compositions of the pectolite at sites 92 and 93 reveal a minor proportion of sulfate and phosphate tetrahedra (Table S11). Grain boundaries are lined with holtstamite, also containing a minor proportion of sulfate and phosphate tetrahedra, as well as fluorine in excess of hydroxyl (sites 88, 89 in Table S16).

The featured exotic mineral analyzed at sites 82 to 85 and 87 in map 30 (Fig. 10a) is a silicate of Ca, Nb, and Ta that contains fluorine and, thus, most likely OH. Of these compositions, the first one in Table S19 has the highest total at 80.2 %; the proportions of Ca, (Nb + Ta) and (Si + Al) are roughly 2 : 2 : 4. This unknown phase, labeled UK2, also contains Zr and Ti at the (Nb + Ta) site. The low totals range from 45 % to 61 %; all of these compositions are relatively depleted in Nb, Zr, and Ti with respect to Ta. The low totals may reflect a poorly polished surface of this hydrous phase or compositions that involve carbonate groups to variable extents. Unknown UK2 is present also in Fig. 10b (map 37), 10c (map 38), and 10f (map 51).

Figure 10c also reveals two grains ∼ 3 µm across of unknown mineral UK1, encountered earlier in Fig. 6e (section MKL-1021). The data on this unknown phase are collated in Table S20. As discussed earlier, there is a very high proportion of sulfur (21 atoms, arbitrarily chosen) with respect to Ca (5–6 atoms) and Sn (2.4 atoms). With so much sulfur, we may be dealing with a sulfide with hydroxide intercalations, similarly to the case of valleriite. A single grain of another late-formed unknown, labeled UK3, is present in map 31 (Fig. 10d). It is found in a cavity in a euhedral crystal of wollastonite, along with aliettite. It is a hydroxyl-bearing silicate of Ca and Nb (Table S21). On the basis of a filled Si site equal to 4, as in komarovite (Pekov et al., 2004), the Ca and (Nb + Ta) sites contain six and seven atoms, respectively. Such proportions differ from the expected values for komarovite and mongolite (Vladykin et al., 1985), the only IMA-approved minerals containing those elements. Also present is diopside with an Mg# value of 95.2.

In map 40 (Fig. 10e), scheelite forms tiny anhedral grains 4 µm across in an assemblage of wollastonite, calcite, pectolite, paragonite, and lawsonite. We report its composition in Table S22. Figure 10f (map 51) shows UK2 (Table S19) coating the rim of cavities in calcite. These may have developed around inclusions of fluorapophyllite-(K) that replaced wollastonite. Also present is diopside with an Mg# value of 96.

5 Discussion

5.1 The intruding magma was evolved and originally granitic

Anorogenic magmatism began near the end of the Paleoproterozoic era in southeastern Finland. The ages of the main units of the Wiborg rapakivi granite batholith are in the range of 1640–1630 Ma, and the associated F-enriched granites are probably younger than 1640 Ma (Vaasjoki, 1977; Rämö et al., 2014; Heinonen et al., 2017). Such evolved

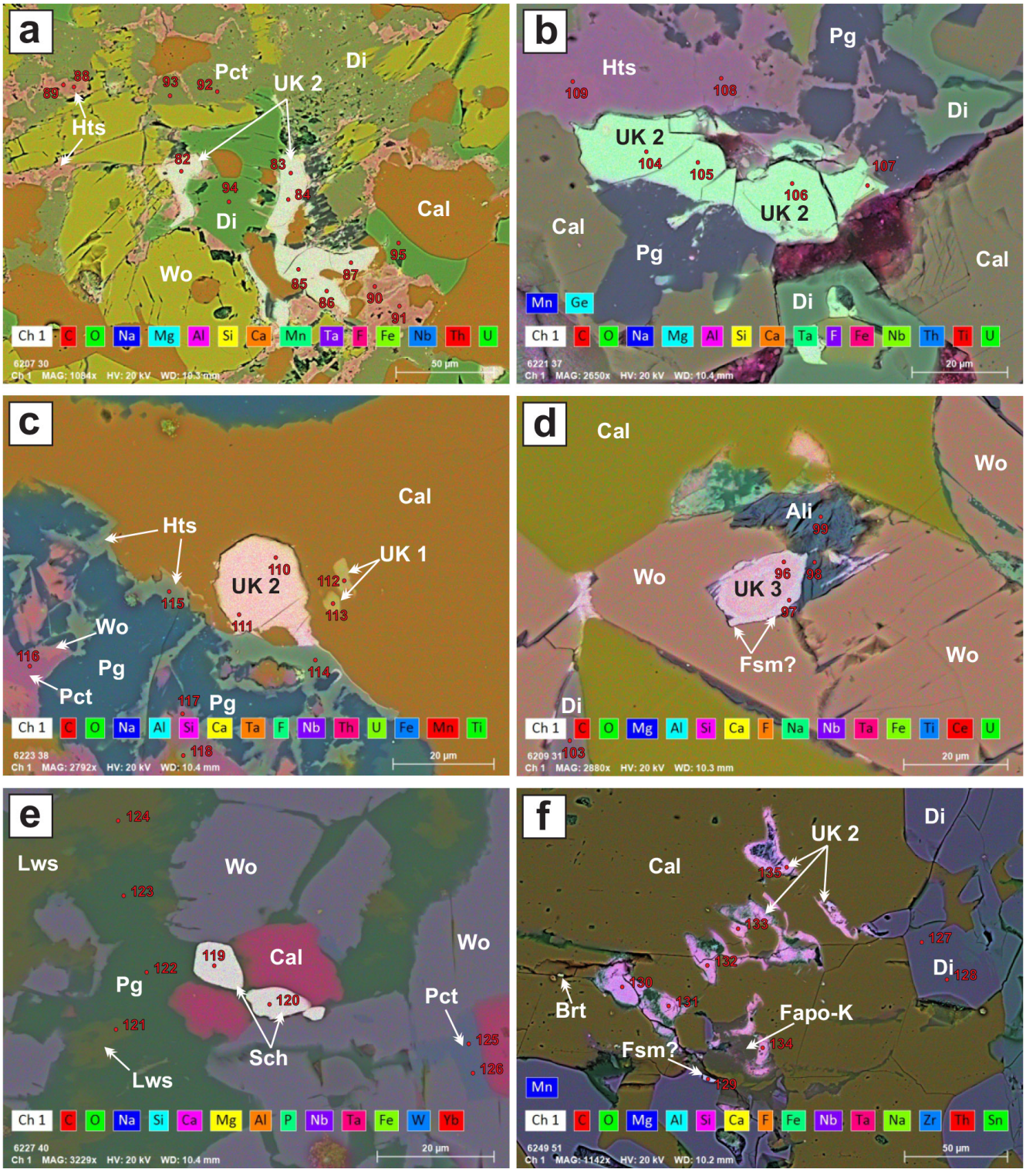

Figure 10. Six maps (**a** to **f**) are selected to illustrate the exotic phases that formed in the dikelets of desilicated igneous material that cut the marble. Some of the exotic phases, labeled UK (i.e., unknown), likely represent new mineral species. Small numbers positioned on some maps mark the site of electron microprobe analyses, the results of which are recorded in Tables S19, S20, and S21. The scale is provided on each map.

rocks make up the Kymi pluton, the best-known example, located roughly 100 km southwest of the Ihalainen deposit. The Kymi topaz granite forms a cupola in the Wiborg batholith. It is enriched in F, Li, Be, Ga, Rb, Sn, and Nb (Haapala and Lukkari, 2005). The biotite in the Kymi topaz granite documents a progressive increase in Si, Li, ^{VI}Al, Mn, Rb, Cs, Zn, Be, Ga, Tl, Ta, and F and a decrease in Fe, Mg, Ti, Ba, Sr, Nb, and Cl as the magma fractionated (Berni et al., 2017). These authors found a decrease in Nb at rather constant Ta in the more evolved granite and associated pegmatite and proposed a selective partitioning of Nb into an aqueous fluid phase to explain it.

At all major occurrences of rapakivi granite, including the Wiborg, Åland, Vehmaa, Laitila, and Ahvenisto massifs in Finland (Vaasjoki, 1977; Rämö et al., 2014) and in the Pitkäranta area of the Salmi batholith in southern Russian Karelia (Konyshev et al., 2020), the composition of the late-formed evolved magmas is F-rich and granitic. Nowhere in the relevant literature is there a mention of a syenitic magma being produced, as is the case locally at Ihalainen. Bodies of episyenites do occur, cutting the Suomenniemi rapakivi granite, north of the Wiborg batholith. These are of metasomatic origin and formed soon after the crystallization of the granite at 1644 Ma (Abersteiner et al., 2025).

A phase-equilibrium investigation of synthetic mixtures simulating the evolved granite of the Kymi pluton (Lukkari and Holtz, 2007) reveals that muscovite is the mineralogical expression of a peraluminous character in a melt containing 2.1 wt % F at 200 MPa and 650 °C, where the fluid phase is H_2O-dominant, or 700 °C, where CO_2 predominates. The F content of the melt should exceed 2.5 wt %–3 wt % to stabilize topaz first and then muscovite at 650 °C at 200 MPa in a H_2O-fluxed melt and in the range of 700–750 °C if the fluid phase contains 50 % CO_2 or more. In melting experiments on a fluorite leucogranite with 1.15 % F from Cornwall, UK, the temperature required to stabilize muscovite and topaz on the liquidus at 200 MPa is 675 °C; muscovite remains stable up to 700 °C at 400 MPa [$P(H_2O = P(total)$] (Weidner and Martin, 1987).

5.2 Turbulence close to the contact with granitic magma (ML-3A)

The magma that intruded the wollastonite ore was evolved and peraluminous. This inference comes from the presence of K-feldspar and muscovite, both enriched in Rb; scheelite; hydroxycalciomicrolite; and unidentified secondary accessory minerals of Sn (UK1, a sulfide), Nb, and Ta (UK2, a silicate) and Nb with Ca (UK3, a silicate). There is no sign of topaz in the dikelet, which indicates only a moderate amount of F in the melt according to Lukkari and Holtz (2007), and no sign of quartz, expected on the basis of all the other occurrences mentioned above.

The dikelet of igneous material consists of an emulsion of silicate and carbonate domains (Fig. 9a). The same comment applies to the chilled margin, in which interconnected domains of carbonate surround the finer-grained silicate minerals. Two largely immiscible melts were present as the emulsion was intruded; they were in intimate contact briefly and then froze. The incoming silicate melt was H_2O-rich, but with insufficient fluorine to produce topaz. On the basis of the above review, a minimum temperature of 675 to 700 °C seems reasonable. Is such a temperature sufficient to melt calcite? Recall that pure calcite undergoes incongruent melting at 645 °C at a $P(H_2O)$ of 100 MPa (Wyllie and Tuttle, 1959; Durand et al., 2015). The binary join $CaCO_3$–H_2O quickly evolves to the ternary system CaO–H_2O–CO_2 during the experiments. Significant decarbonation thus accompanies the "wet" melting of calcite. In the presence of H_2O, the solidus is likely to be near-vertical in a P–T plot. Additional fluxes like fluorine, sulfur, and phosphorus lower the solidus of the carbonate melt. Deeper in the crust, at 1 GPa, a hydrous carbonate melt coexists with magnesian calcite and dolomite at 825 ± 25 °C (Liu et al., 2025); the presence of fluorine would lower that minimum temperature (Gittins and Tuttle, 1964).

Before the actual injection of the dikelet, a desilication reaction must have taken place in the area, between a viscous silica-oversaturated felsic melt and a fluxed runny carbonate melt in which the activity of silica was very low. One can visualize a vigorous reaction in a turbulent setting in which globules of disaggregated granitic melt mingled with the carbonate melt. Vigorous stirring favored the reaction to reduce the major imbalance in silica activity. The carbonate melt, itself a powerful flux, dissolved the adjacent silicate melt selectively and, evidently, partly desilicated it to the extent that it efficiently became a feldspathic melt, poised to crystallize alkali feldspars without quartz or a feldspathoid. On a small scale, the vigorous mingling of silicate and carbonate melts likely resembled that in the Early Paleozoic Ol'khon collision system in the West Baikal system of Russia (Sklyarov et al., 2013).

The silicocarbonatitic melt at the contact of the dikelet crystallized a new generation of wollastonite and very minor diopside (Fig. 9a). The skeletal nature of some of the neoformed wollastonite suggests rapid crystallization, presumably owing to efficient degassing of the assemblage. A compact polycrystalline enclave of wollastonite (Fig. 9g) suggests the likelihood that a wollastonite cumulate could form in the carbonate melt. This fragment of cumulate was eventually entrained in the more viscous silicate melt (Fig. 9h).

The resulting feldspathic melt crystallized a single calcium-poor alkali feldspar (sanidine solid solution). The minimum temperature of an H_2O-saturated feldspathic melt on the join Ab–Or is 865 °C at 100 MPa, 800 °C at 200 MPa, and 765 °C at 300 MPa (Tuttle and Bowen, 1958, Fig. 17). A small amount of Ca in the melt and a dilution of the aqueous fluid with CO_2 would raise the solidus temperature. Counteracting these factors is the F content of the evolved feldspathic melt. We believe that the temperatures quoted are realistic.

As the system cooled, exsolution is expected to occur as the feldspar crosses the dome of unmixing, but which dome will it be? There are two possibilities. Exsolution may occur by nucleation and growth or by spinodal decomposition. The first produces the familiar perthitic intergrowth of lenticular strands of sodic feldspar in a K-feldspar host expected in cases of strain-free exsolution in the presence of H_2O. Smith and Brown (1988, Fig. 1.2a) showed the crest of the strain-free solvus at approximately 675 °C at a low pressure. The crest of the solvus is relatively insensitive to confining pressure.

Spinodal decomposition of a sanidine solid solution, much less frequently encountered, occurs at a lower temperature than in the previous case (Smith and Brown (1988, Fig. 19.1a) and involves interdiffusion of Na and K atoms in the interstices of the aluminosilicate framework in a relatively dry environment. The Al and Si cations remain in place in the structure. The Na and K, initially homogeneously distributed across a crystal, develop a sinusoidal pattern of Na-rich and K-rich domains by intracrystalline diffusion. The structure of the K- and Na-rich domains remains coherent with respect to the framework, and the two exsolved feldspars are strained as a result. As there is no nucleation barrier to be overcome during spinodal decomposition, the process is considered to be relatively rapid compared to nucleation and growth of strain-free phases (Abart et al., 2009). At Ihalainen, this fact, combined with protracted slow cooling of the batholith and a fluid phase that was CO_2-dominant at the stage of exsolution, produced an unusually well-developed "neural" network of intergrown domains of albite and K-feldspar (Fig. 9b–f). In these figures, we recognize both the stripe and island-to-labyrinthine patterns imaged by Sánchez-Muñoz et al. (2016, Fig. 3). As those authors pointed out, spinodal decomposition is a phase separation phenomenon occurring under non-equilibrium conditions.

Once the unusual pattern of exsolved feldspars had formed in response to the coherent solvus, at a temperature probably in the range of 550–500 °C, intracrystalline diffusion became inefficient. The fluid phase eventually became H_2O-dominant as temperature decreased. We contend that strain was eventually removed from the strained structures by solution and redeposition, but the tell-tale texture of spinodal decomposition was not destroyed by this recrystallization. Whether the influx of H_2O induced Al–Si order in the K-rich feldspar remains untested. Elsewhere in the Wiborg rapakivi massif, Vorma (1971) showed that both relict orthoclase and well-ordered microcline are present. The sodic feldspar is expected to have become fully ordered quickly (Martin, 1969). Many hydrous phases then appeared; pectolite (Fig. 9a, e, f, g), paragonite (Fig. 9a, b, d, e, f), holtstamite (Fig. 9b, d, g, h), lawsonite (Fig. 9b, d), prehnite (Fig. 9b, e) gonnardite (Fig. 9h), and xonotlite (Fig. 9h) have been tentatively identified on the basis of their energy dispersion spectrum. The exotic minerals of Sn, Nb, and Ta (Fig. 10) grew at a late stage from the aqueous fluid phase.

5.3 Distal interaction with the intruding magma (MKL-1021)

Section MKL-1021 also provides clear evidence of a melt but of a highly unusual composition, encountered here for the first time. In this case, quartz is absent in the dikelet, as in the previous case, and feldspar is generally absent as well (Figs. 6a–c). The melt crystallized to wollastonite + forsterite + fluorite + diopside in a location near the intruding granite and possibly above it. The evidence favoring melting comes from the presence of a graphic intergrowth of wollastonite and fluorite. Both grew simultaneously in a pocket of melt with a composition in the system of CaO–MgO–SiO_2–H_2O–F. Upon emplacement, this melt crystallized either wollastonite or fluorite or diopside on the wall of the pocket, in contact with calcite. Once this envelope was created, the residual melt went on to crystallize forsterite, and the fractionated melt congealed as a graphic intergrowth of wollastonite and fluorite. The melt quenched as it came in contact with the carbonate matrix.

The inferred presence of forsterite does not imply that the assemblage is ultrabasic. Rather, it reflects the inability of wollastonite and fluorite to accept Mg. The low activity of silica in the melt favored forsterite rather than enstatite. Here, there is more Mg than in the previous case, an indication of the greater modal amount of diopside in the volume of wollastonite ore that was affected. The forsterite reacted completely with an aqueous fluid at a low temperature to give aliettite, compositionally similar to lizardite. Note that lizardite is widespread in the deposit, particularly in dolomitic marble (Lehtinen, 1995).

The symplectic texture implies that fluorite and wollastonite crystallized simultaneously and interfered with each other as they grew from the melt. In a domain of symplectite, strands of the two minerals are oriented more or less perpendicularly to forsterite (now aliettite), which had crystallized earlier (Fig. 6b). Also present and formed as part of the intergrowth are scheelite, fluorapatite (Fig. 6b), and malayaite (Fig. 6d).

The system $CaSiO_3$–CaF_2, investigated at one atmosphere in connection with slag formation in the steel industry, shows a binary eutectic at 1127 °C, with the eutectic melt containing 41 % $CaSiO_3$ (molar basis: Bååk and Ölander, 1955). There is no information on the ternary system $CaSiO_3$–CaF_2–H_2O. We can expect a significant lowering of the eutectic temperature in the pseudobinary system, likely close to 800 °C.

We do know that the wollastonite ore at Ihalainen does not contain much fluorite. Lehtinen (1995) reported that only five samples (12.8 % of the data) have F contents greater than or equal to 0.05 wt %, the limit of quantification. Three of these were from the southern end of the quarry, where the influence of a pegmatite dike on the marble was most significant.

The peak concentration (0.14 wt %) corresponds to 0.29 wt % fluorite.

We propose that fluorite was added to the wollastonite ore locally by a fluid phase emanating from the subjacent body of Wiborg F-enriched granite. The solubility of CaF_2 in H_2O increases strongly with increasing P and T in experiments at 600 °C and above between 0.5 and 2 GPa (Tropper and Manning, 2007). The mineral dissolves congruently. In a temperature gradient, one can propose that fluorite was locally deposited by vapor transport in the ore assemblage. There is no more efficient mode of heat transfer than the advection of a fluid phase. Melting occurred once fluorite and heat were added to the affected portion of the ore. Also transported by vapor transport are tin and tungsten, needed to form malayaite and scheelite.

The circulation of a calcic aqueous fluid continued as the assemblage cooled. Fluorapophyllite-(K) is a prominent product of the alteration of wollastonite (Fig. 6a, b, c, f, g). Specks of cassiterite are embedded in fluorapophyllite-(K) (Fig. 6, map 34). Tin also appears as unknown mineral UK1 (Fig. 6e, map 25), a sulfide of Ca and Sn, inferred to have been deposited from a fluid phase in a partly dissolved region of the matrix. In one area of section MKL-1021 (map 19, Fig. 6h), we find a millimetric grain of K-feldspar + albite containing traces of diopside and fluorite. The grain likely has a detrital origin. It was partially replaced by Ca-bearing hydrous phases [holtstamite, katoite (?), aliettite]. The aqueous phase circulating at the subsolidus stage was dominantly calcic owing to the solubility of calcite and fluorite (Caciagli and Manning, 2003; Tropper and Manning, 2007).

6 Conclusions

The juxtaposition of a mineralized block of marble and granitic magma led to anatectic reactions affecting the marble, followed by turbulent mixing of the two melts, at least on a local scale. Our observations concerning the interaction offer a first look at the phenomenon that led to enrichment of the wollastonite ore. The invading granitic magma was efficiently desilicated during the magma-mixing event, and the carbonate melt became silicocarbonatitic owing to its aggressivity as a flux. The calcium-poor syenitic melt crystallized metastably in the presence of a carbothermal fluid to a single alkali feldspar (sanidine) that unmixed by spinodal decomposition. The textural evidence is exceptionally well displayed at Ihalainen. We have demonstrated the creation of a melt in the system $CaSiO_3$–CaF_2–$CaMgSi_2O_6$–H_2O as a result of the gaseous infiltration of CaF_2 emanating from the adjacent or subjacent pluton into the ore zone. The striking graphic intergrowth of wollastonite + fluorite coexists with forsterite (now aliettite). Its presence reflects their rejection of magnesium derived from diopside in the ore. We will clearly need larger crystals of the three unknown exotic species UK1, UK2, and UK3 to proceed to an IMA submission. In view of the relative enrichment of the Wiborg batholith in high-field-strength elements, more such discoveries can be expected at Ihalainen.

Data availability. All the data available are in this article. Specifically, from the two URL addresses provided above, one can retrieve all element-distribution maps, all energy-dispersion spectra and all analytical data that were acquired. To repeat, these URL addresses are (1) https://petapixelproject.com/mosaics/geology/Ihalainen/MKL-1021-BBV/index.html and (2) https://petapixelproject.com/mosaics/geology/Ihalainen/ML-3A-BBV/index.html.

Supplement. The supplement related to this article is available online at https://doi.org/10.5194/ejm-38-431-2026-supplement.

Author contributions. RFM and DS prepared the text, table, and figures. MJL provided the specimens described here, as well as details about their provenance, geological context, and mineralogical composition; valuable feedback; and Fig. 1. SF acquired the quantitative compositional data reported here. All of the authors have gone over the text.

Competing interests. The contact author has declared that none of the authors has any competing interests.

Disclaimer. Publisher's note: Copernicus Publications remains neutral with regard to jurisdictional claims made in the text, published maps, institutional affiliations, or any other geographical representation in this paper. The authors bear the ultimate responsibility for providing appropriate place names. Views expressed in the text are those of the authors and do not necessarily reflect the views of the publisher.

Acknowledgements. Markku Lehtinen thanks Nordkalk Oy Ab and SigmaRoc PLC, as well as his colleagues at Ihalainen in the 1990s and 2000s for the practical assistance provided. These include Vice President and Director Eelis Eskelinen and Mine Manager Tauno Paalumäki, both deceased. We have sought and received permission to publish from Nordkalk Corporation. We thank Simon Gold and Christian Wöhrl for their support with the electron microprobe analyses. This investigation began with a focus on the cause of the blue coloration in calcite. We are grateful for a sample of blue calcite from Ihalainen, collected by the late Werner Schreyer and sent to us by Hans-Peter Schertl of the Ruhr-Universität Bochum. Further samples caused us to shift our focus to the petrological issues reported here. We are grateful to an anonymous referee, Dr. Tapani Rämö, associate editor Dewashish Upadhyay, and editor Elisabetta Rampone for their helpful suggestions for improvement. We thank the editorial staff for their assistance.

Review statement. This paper was edited by Dewashish Upadhyay and reviewed by Jakub Jirásek and Tapani Rämö.

References

Abart, R., Petrishcheva, E., Wirth, R., and Rhede, D.: Exsolution by spinodal decomposition. II. Perthite formation during slow cooling of anatexites from Ngoronghoro, Tanzania, Am. J. Sci., 309, 450–475, https://doi.org/10.2475/06.2009.02, 2009.

Abersteiner, A., Rämö, O. T., Kontonikas-Charos, A., Kharkongor, M., Karampelas, N., Gilbert, S. E., Wade, B., Ambroziak-Murzyn, K., Lloyd, J. C., Beier, C., and Glorie, S.: Timing of episyenite formation in the Proterozoic Suomenniemi rapakivi granite complex (Finland), Lithos, 516–517, 108269, https://doi.org/10.1016/j.lithos.2025.108269, 2025.

Bååk, T. and Ölander, A.: The system $CaSiO_3$–CaF_2, Acta Chem. Scand., 9, 1350–1354, 1955.

Bailey, S. W.: A system of nomenclature for regular interstratifications, Can. Mineral., 19, 651–655, 1981.

Berni, G. V., Wagner, T., Fusswinkel, T., and Wenzel, T.: Magmatic-hydrothermal evolution of the Kymi topaz granite stock, SE Finland: mineral chemistry evidence for episodic fluid exsolution, Lithos, 292, 401–423, https://doi.org/10.1016/j.lithos.2017.09.015, 2017.

Caciagli, N. C. and Manning, C. E.: The solubility of calcite in water at 6–16 kbar and 500–800 °C, Contrib. Mineral. Petr., 146, 275–285, https://doi.org/10.1007/s00410-003-0501-y, 2003.

Durand, C., Baumgartner, L. P., and Marquer, D.: Low melting temperature for calcite at 1000 bars on the join $CaCO_3$–H_2O – some geological implications, Terra Nova, 27, 364–369, https://doi.org/10.1111/ter.12168, 2015.

Gittins, J. and Tuttle, O. F.: The system CaF_2–$Ca(OH)_2$–$CaCO_3$, Am. J. Sci., 262, 66–75, 1964.

Haapala, I. and Lukkari, S.: Petrological and geochemical evolution of the Kymi stock, a topaz granite cupola within the Wiborg rapakivi batholith, Finland, Lithos, 80, 347–362, https://doi.org/10.1016/j.lithos.2004.05.012, 2005.

Heinonen, A. P., Rämö, O. T., Mänttäri, I., Andersen, T., and Larjamo, K.: Zircon as a proxy for the magmatic evolution of Proterozoic ferroan granites; the Wiborg rapakivi granite batholith, SE Finland, J. Petrol., 58, 2493–2517, https://doi.org/10.1093/petrology/egy014, 2017.

Kilpeläinen, T. and Rastas, J.: Tectonic-metamorphic investigations in the surroundings of Telkkälä Ni deposit, Institute of Geology and Mineralogy, University of Turku, Publication, 29, [accessible at library@gtk.fi], 1992 (in Finnish).

Konyshev, A. A., Chevychelov, V. Y., and Shapovalov, Y. B.: Two types of highly differentiated topaz-bearing granites of the Salmi batholith, southern Karelia, Geochem. Int., 58, 11–26, https://doi.org/10.1134/S0016702920010073, 2020.

Lehtinen, M. J.: Lappeenrannan Ihalaisten muodostuman mineralogiasta ja geologiasta (On the Geology and Mineralogy of Ihalainen Formation in Lappeenranta), Ph.lic. thesis, University of Turku, Turku, Finland, [accessible at library@gtk.fi], 1995 (in Finnish).

Lehtinen, M.J.: The crystalline limestone deposits of Ihalainen (Lappeenranta) and Louhi (Kerimäki) in SE Finland and their production history, in: Industrial Minerals: Deposits and New Developments in Fennoscandia. Karelian Research Center, Russian Academy of Sciences, Petrozavodsk, Russia (41–43), [accessible at library@gtk.fi], 1999.

Liu, P., Massonne, H.-J., Wei, C., Lu, Y., and Lu, W.: Melting relationships of calcite – dolomite – H_2O at 1 GPa and implications for partial melting of metacarbonate rocks in deeply buried crust, J. Petrol., 66, egaf061, https://doi.org/10.1093/petrology/egaf061, 2025.

Lukkari, S. and Holtz, F.: Phase relations of a F-enriched peraluminous granite: an experimental study of the Kymi topaz granite stock, southern Finland, Contrib. Mineral. Petr., 153, 273–288, https://doi.org/10.1007/s00410-006-0146-8, 2007.

Martin, R. F.: The hydrothermal synthesis of low albite, Contrib. Mineral. Petr., 23, 323–339, 1969.

Pekov, I. V., Azarova, Y. V., and Chukanov, N. V.: New data on komarovite series minerals, New Data on Minerals, 39, 5–13, 2004.

Pekov, I. V., Sereda, E. V., Zubakova, N. V., Yapaskurt, V. O., Chukanov, N. V., Britvin, S. N., Lykova, I. S., and Pushcharovsky, D. Y.: Genplesite, $Ca_3Sn(SO_4)_2(OH)_6{\cdot}3H_2O$, a new mineral of the fleischerite group: first occurrence of a tin sulfate in nature, Eur. J. Mineral., 30, 375–382, 2018.

Rämö, O. T.: Petrogenesis of the Proterozoic rapakivi granites and related basic rocks of southeastern Fennoscandia: Nd and Pd isotopic and general geochemical constraints, Geological Survey of Finland, Bulletin, 355, [accessible at library@gtk.fi], 1991.

Rämö, O. T., Turkki, V., Mänttäri, I., Heinonen, A., Larjamo, K., and Lahaye, Y.: Age and isotopic fingerprints of some plutonic rocks in the Wiborg rapakivi granite batholith with special reference to the dark wiborgite of the Ristisaari Island, B. Geol. by Bull. Geol., 86, 71–91, https://doi.org/10.17741/bgsf/86.2.002, 2014.

Sánchez-Muñoz, L., Del Campo, A., and Fernández, J. F.: Symmetry constraints during the development of anisotropic spinodal patterns, Scientific Reports, 6, 1–10, https://doi.org/10.1038/srep20806, 2016.

Simonen, A.: Geological Map of Finland (1 : 100 000). Pre-Quaternary Rocks, Sheet 3133, Ylämaa, Geological Survey of Finland, Espoo, Finland, [accessible at library@gtk.fi], 1979.

Sklyarov, E. V., Fedorovsky, V. S., Kotov, A. B., Lavrenchuk, A. V., Muzakabzov, A. M., and Starikova, A. E.: Carbonate and silicate–carbonate injection complexes in collision systems: the West Baikal region as an example, Geotectonics, 47, 180–196, https://doi.org/10/1134/S0016852113020064, 2013.

Smith, J. V. and Brown, W. L.: Feldspar Minerals. 1. Crystal Structures, Physical, Chemical, and Microtextural Properties, Springer-Verlag, Berlin, Germany, ISBN 3-540-17692-6, 1988.

Tropper, P. and Manning, C. E.: The solubility of fluorite in H_2O and H_2O–NaCl at high pressure and temperature, Chem. Geol., 242, 299–306, https://doi.org/10.1016/j.chemgeo.2007.03.017, 2007.

Tuttle, O. F. and Bowen, N. L.: Origin of granite in the light of experimental studies in the system $NaAlSi_3O_8$–$KAlSi_3O_8$–SiO_2–H_2O, Geol. Soc. Am. Mem., 74, https://doi.org/10.1130/MEM74, 1958.

Vaasjoki, M.: Rapakivi granites and other postorogenic rocks in Finland; their age and the lead isotopic composition of certain associated galena mineralizations, Geological Survey of Finland, Bulletin, 294, [accessible at library@gtk.fi], 1977.

Veniale, F. and van der Marel, H. W.: Identification of some 1 : 1 regular interstratified trioctahedral clay minerals, Proceedings of the International Clay Conference (Tokyo), 1, 233–244, 1969.

Vladykin, N. V., Drits, V. A., Kovalenko, V. I., Dorfman, M. D., Malov, V. S., and Gorshkov, A. I.: A new silicate of niobium – mongolite $Ca_4Nb_6[Si_5O_{20}]O_4(OH_{10})\cdot nH_2O$ [sic], Zapiski Vsesoyuznogo Mineralogicheskogo Obshchestva, 114, 374–377, 1985 (in Russian).

Vorma, A.: Geological Map of Finland (1 : 100 000). Pre-Quaternary Rocks, Sheet 3134, Lappeenranta, Geological Survey of Finland, Espoo, Finland, [accessible at library@gtk.fi], 1964.

Vorma, A.: Alkali feldspar of the Wiborg rapakivi massif in southeastern Finland, Bulletin de la Commission Géologique de Finlande, 246, [accessible at library@gtk.fi], 1971.

Vorma, A.: On two roof pendants in the Wiborg rapakivi massif, southeastern Finland, Geological Survey of Finland, Bulletin, 272, [accessible at library@gtk.fi], 1975.

Weidner, J. R. and Martin, R. F.: Phase equilibria of a fluorine-rich leucogranite from the St. Austell pluton, Cornwall, Geochim. Cosmochim. Ac., 51, 1591–1597, 1987.

Wyllie, P. J. and Tuttle, O. F.: Melting of calcite in the presence of water, Am. Mineral., 44, 453–459, 1959.